Supporting information

Phytogenic rGO@$ZnCo_2O_4$ Spinel Nanoarchitecture for Solar-Induced Detoxification of Endocrine Disruptors: Interface Engineering and Charge Carrier Modulation

Bharti Agarwal[1], Manviri Rani[1]*, Uma Shanker[2]*

[1] Department of Chemistry Malaviya National Institute of Technology Jaipur, Jaipur, Rajasthan, India-302017

[2]Department of Chemistry Dr. B R Ambedkar National Institute of Technology Jalandhar, Jalandhar, Punjab, India-144008

* Corresponding Author

Dr. Manviri Rani

Department of Chemistry

Malaviya National Institute of Technology Jaipur,

Jaipur, Rajasthan, India-302017

Email: manviri.chy@mnit.ac.in

Contact number: +91- 9549-650-291 (Mobile)

Dr. Uma Shanker

Department of Chemistry

Dr. B R Ambedkar National Institute of Technology Jalandhar,

Jalandhar, Punjab, India-144008

Email: shankeru@nitj.ac.in, umaorganic29@gmail.com

Contact number: +91- 7837-588-168 (Mobile)

Text S1: Synthesis details

2.1 Preparation of *A. indica* leaf extract

Deionized water was used to wash the *A. indica* leaves and then dry them. Nearly, 5 g of leaves were mixed with water, crushed in a pestle and mortar, and then filtered. For synthesis use, the PE solution was stored at 4°C. *A. indica* is significant source of quercetin-3-glucoside, galic acid, and polyhydroxy flavonoids, they also contain many polyphenols. The presence of phenols (4.25 0.04%), flavonoids (7.43 0.03%), glycosides (0.11 0.01%), alkaloids (1.90 0.01%), tannins (0.86 0.02%) and saponins (2.50 0.01%), in *A. indica* leaves extract has also been established.[S1] Fig. 1S shows the tentative mechanism of formation of nanomaterials synthesized by the using A. indica leaves extract. The interfacial tension was decreased by these phytochemicals to regulate particle development. The presence of toxic and hazardous reducing or stabilizing agents (sodium borohydride, cetyltrimethylammonium bromide, ethylenediaminetetraacetic acid) in chemical methods makes them unfavourable for the environment. To overcome such problems, green synthesized nanomaterials (safer, more sustainable, and efficient) using plants extracts are in demand.[S2] Literature revealed that polyols (e.g., polyphenols, flavonoids, and glycosides) are actually responsible for the reduction of metal ions (III) ions, whereby they themselves get oxidized to an α,β-unsaturated carbonyl group as shown in Figure below. Polyphenols, flavonoids and glycosides firstly reduced the metallic ions and then stabilizing them by adhering on the surface of the nanoparticles formed. Saponins, and alkaloids reduced the probability of agglomeration to control the particle size.[S2] Hydroxyl group of flavonoids and polyphenols act as capping agent and stabilize the synthesized NPs. The hydroxyl and carbonyl groups present in amino acid residue or in protein act as capping agent reduce agglomeration of NPs and stabilize them [Fig. 1S].

$NADH \longrightarrow NADH^{\cdot+} + e^{-}$ electron transfer

$NADH^{\cdot+} \longrightarrow NAD^{+} + H^{+}$ chemical reaction

$NAD^{\cdot} \longrightarrow NAD^{+} + e^{-}$

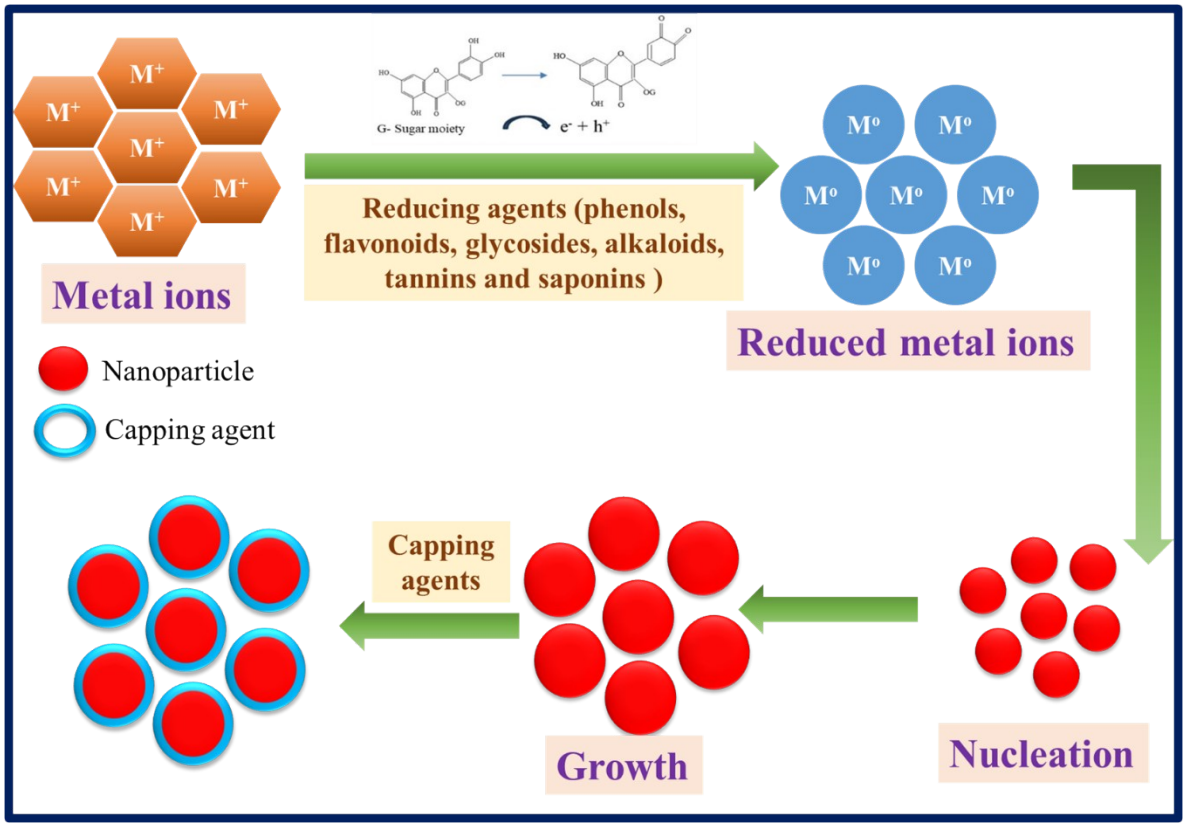

Fig 1S: Tentative mechanism of formation of nanomaterials synthesized by the using *A. indica* leaves extract·

2.2 Thermal method-based synthesis of reduced graphene oxide (rGO)

Graphene oxide was synthesized using a modified Hummer's method,[S3] which consists of a mixture of 2g graphite powder and 2g $NaNO_3$ with conc. H_2SO_4 solution (50mL) was continuously stirred in an ice bath for about one hour, then slowly added 6g of $KMnO_4$ with vigorous stirring, maintaining the temperature of the reaction chamber below 15 °C for about 3 h. A brown color paste was obtained, and 150mL of deionized water was mixed and stirred for about 30 minutes at 95 °C. After that, 100 deionized water was added to the dilute solution by treating it with 10mL H_2O_2. After some hours, a brownish-yellow solution was obtained and washed using dil. HCl and deionized water to maintain pH 7. The obtained residue was

graphene oxide which was filtered and dried in an oven overnight at 60 °C. Then, this graphene oxide was annealed using a Scientific SMFF-3S-230V Muffle oven for about 3 h at 350 °C and allowed to cool until room temperature to obtain black-colored reduced graphene oxide powder. The graphene oxide is converted into reduced graphene oxide (rGO) by direct heating in a furnace (inert atmosphere) by thermal method, so persuading the elimination of most of the graphene oxide functional groups such as hydroxyl, epoxide, carboxyl, and carbonyl.[S4]

Fig 2S shows the schematic diagram of rGO.

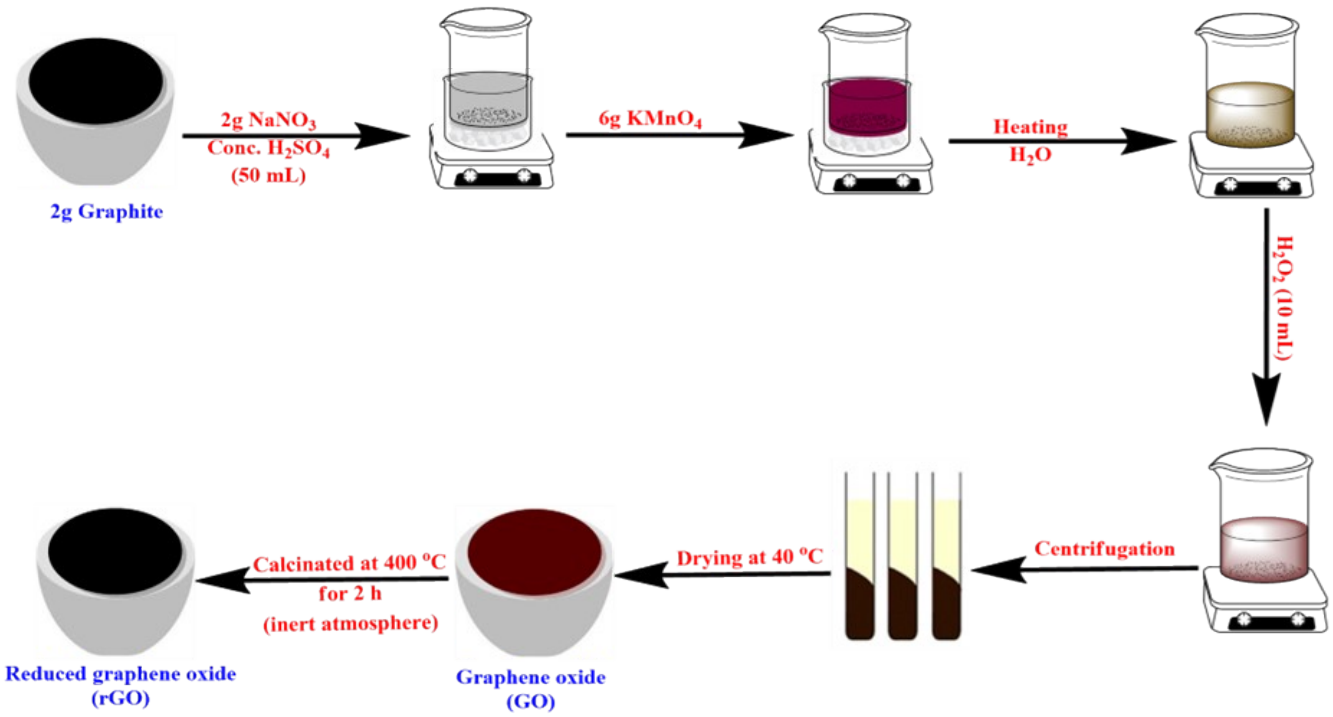

Fig 2S: Schematic representation for the synthesis of rGO

Text S2: Instrumentation

The materials underwent PXRD analysis utilising a PAN analytical X-PRT PRO apparatus from the USA and CuKa radiation with λ = 1.5406 A°. Powdered samples (properly ground and symmetrically dispersed) were put in the sample holder in a coplanar pattern. FT-IR experiments using an Agilent Cary 630 FTIR spectrometer (USA) confirmed the existence of several functional groups and bonds produced in the doped nanocomposite. Unlike standard

FT-IR, which uses KBr as a reference, this approach requires no particular sample preparation or reference material. The synthesised nanoparticles' infrared spectra ranged from 400 to 4000 cm^{-1} (Agilent ATR model). The surface morphology of produced samples was determined using a field emission gun equipped FEI-Nova Nano SEM 450 microscope (Kensington UNSW Sydney NSW 2052). The element weight percentage in the sample was estimated using electron dispersive spectroscopy. The EI ion source has been configured to operate at 350 degrees Celsius. ESCA+ omicron nanotechnology Oxford instruments were used to perform an X-ray photo electron spectroscopy (XPS) measurement. The Brunauer-Emmett-Teller (BET) specific surface area was determined by nitrogen adsorption-desorption isotherm analysis utilising SMART Instruments, SMART SORB 93 model, following degassing at 150°C for 3 hours. The stability of the photocatalyst was assessed by measuring the zeta potential with the Malvern Zetasizer (Version 7.11). The band gap was calculated by acquiring Diffuse Reflectance Spectra data from a Shimadzu UV-Vis spectrometer and translating it to Tauc's plot. Band gap energy (Eg) and semiconductor absorption coefficient are associated through Eq (1), with n values depending on the nature of the transition.

$$\alpha = \frac{C(hv - E_g)^n}{hv} \tag{1}$$

The EIS study was conducted by CHI 7087E instrument with frequency range 0.01Hz to 10^5 Hz at the amplitude of 0.01 V. In addition, CPA-225D Sartius Analytical balance was used for weighing purpose and LABWAN –PH-61WW instruments was used for the preparation of pH solutions total organic carbon (TOC) analysis by the TOC -L analyser Shimazu.

Text S3: Analytical methods

The concentration of PAEs in treated solutions was determined using an HPLC (Agilent 1200, Agilent, USA) with a UV detector at 230 nm. An amethyst C18-P column (5µm, 4.6 155 × 150 mm) was used as a separation column. The mobile phase was a mixture of methanol and water

(80:20, v/v) with a flow rate of 0.8 min mL^{-1} and injection volume = 10 µL, total run time of 20 min. Aqueous samples were taken at 0, 30, 60, 90, and 120, 150, 180 minutes and analysed using an HPLC. For the identification of degradation products, the samples were injected into the liquid chromatograph (LC 1300) coupled with a mass spectrometer (TSQ8000) with the electron ionization mode. The dimensions of the column (TG 5MS) were 30 m 0.25 mm i.d.0.25 mm film thickness. The carrier gas was helium having a flow rate of 2 ml min^{-1}. The conditions for LC were: injector temperature, 180 °C, and transfer line temperature, 150 °C. The capillary column temperature was programmed to 60°C for 12 min; from 60 to 160 °C at 10 °C min^{-1} and holding for the next 15 min. Chromatographic data was collected by capturing full scan mass spectra in the m/z range of 50 to 500. Mass spectra used to detect chromatographic peaks were interpreted directly based on fragments. The degradation mechanism of PAEs was hypothesised based on the structures of the byproducts of the respective m/s data, which matched the NIST library and literature. The total organic carbon (TOC) of aqueous samples was analyzed by a TOC analyser (Aurora 1030 W, OI Analytical, USA) by the heated persulfate wet oxidation.

Text S4: Statistical analysis

The reaction kinetics, rate constants and best fit plots for removing PAEs from nanocatalyst surfaces were empirically examined using Sigma plot ver. 10.0 software (SPSS). Standard deviation was calculated using Microsoft excels program which shows better results with triplicate samples. The results were then supported by Regression of coefficient (R^2) and p-value (≥ 0.05). For adsorption data analysis, several models were used (Langmuir isotherm, Freundlich, Dubinin-Radushkevich (DRK) and Temkin isotherm). A straight line ($Y= mX + c$) linear curves have been plotted for adsorption isotherms at different concentrations.

Details of Langmuir, Freundlich, Temkin, Sip and D-R isotherms used in present study

Adsorption data through Langmuir adsorption isotherms were calculated through graph of Ce/Xe v/s Ce of the solute. Which were calculated by fitting the adsorption data into the equation:

$$\frac{C_e}{X_e} = \frac{1}{k_L X_m} + \frac{C_e}{X_m}$$

or

$$\frac{1}{X_e} = \frac{1}{C_e}\left(\frac{1}{k_L X_m}\right) + \frac{1}{X_m}$$

$X_e$was calculated through the equation:

$$X_e = \frac{(Ci - Ce) \times Volofsolution(mL) \times Molecularweightofadsorbent}{Amountofcatalyst\ (mg)}$$

Fruendlich Isotherm.

A typical graph of Xe v/s Ce of the solute was a straight line. $Xe = Kf + Ce1/n$ and linear form is

$$\log Xe = \log Kf + \frac{1}{n} logCe$$

Where C_e is the equilibrium concentration of the dye solution; X_e is the amount of dye adsorbed per gram weight of adsorbent; Kf is the Freundlich adsorption constant (mg/g); n is adsorption intensity.

Temkin Isotherm:

$$Xe = \frac{RT}{b} \ln A + \frac{RT}{b} \ln Ce$$

Where B=RT/b constant related to heat of sorption (J/mol) obtained from the Temkin plot (qeVslnCe); A (slope) = Temkin isotherm equilibrium binding constant (L/g); b (intercept) =

Temkin isotherm constant; *R* =universal gas constant (8.314 J·mol−1·K−1) *T* = Temperature at 298, 308 and 318 K.

As C_e values were very low, the $\ln C_e$ values were coming out to be negative. Therefore, Temkin isotherm (X_e v/s $\ln C_e$) was not plotted for present study.

Dubinin-Radushkevich (D-R) isotherm:

$$\ln Xe = \ln Xm - \beta\varepsilon 2$$

$$\varepsilon = RTln\left(1 + \frac{1}{Ce}\right)$$

Where X_m is maximum adsorption capacity (mg/g) obtained from intercept; β (mol^2/J^2) is a activity coefficient constant related to sorption energy and obtained from slope; ε is Polanyi potential. D-R was plotted between lnXeVs ε^2.

Sips Isotherm

It is plotted between 1/Xe $\times 10^{-2}$ (g/mg) and (1/Ce) $\times 10^{-8}$ L/mg; where (1/mg) and (mg/g) are the Sips equilibrium constant and maximum adsorption capacity values obtained from the slope and the intercept of the plot. The Sips isotherm equation is characterized by the dimensionless heterogeneity factor 'n' which can also be employed to describe the system's heterogeneity when is between 0 and 1.

$$\frac{1}{X_e} = \frac{1}{XmKs}\left(\frac{1}{Ce}\right)1/n + \frac{1}{X_m}$$

Equation used for calculation Band Gap Energy values

The optical band gaps were estimated by converting reflectance data to absorption spectra using the Kubelka–Munk function $F(R_\infty)$, as shown in Eq. (4).

$$(F(R_\infty) \times h\nu)^n = B\,(h\nu - E_g) \quad (4)$$

Planck's constant (h), photon frequency (ν), the proportionality constant (B), and band gap energy (E_g) define the Tauc relation, where the exponent n indicates the transition type, n = ½

for direct and n = 2 for indirect allowed transitions. Band gap energies were estimated from Tauc plots i.e., $(F(R\infty)\times h\nu)^n$ vs. hν] using n = ½, as shown in Fig. 5e.The Urbach region was identified by plotting (ln(F(R)) vs. hν) versus photon energy and fitting the low-energy linear segment.[S5]

E_U = 1/slope

Thus, E_U and E_g quantify distinct phenomena: E_U measures the energetic width of disorder-induced tail states that increase sub-gap absorption, whereas E_g represents the band-to-band transition energy. The coexistence of a modestly reduced E and a substantial E_U rationalizes the enhanced visible-light absorption and charge-transfer behavior observed for rGO@$ZnCo_2O_4$.

Tables and Figures

Table 1S. Details of angle, FWHM values, interplanar spacing and hkl values of rGO@ $ZnCo_2O_4$, rGO and $ZnCo_2O_4$ respectively

a. rGO@$ZnCo_2O_4$

Angle (2θ)	FWHM value	d-spacing (A^0)	hkl values
19.11	0.08364	4.64367	(111)
28.02	0.1428	3.1816	(002)
32.13	0.5353	2.78287	(220)
37.16	0.3011	2.43007	(311)
39.79	0.2676	2.289	(222)
44.97	0.5353	2.14372	(400)
56.79	0.1632	1.61991	(422)
59.37	0.2676	1.55519	(511)
65.25	0.4684	1.42838	(440)

68.24	0.1632	1.3743	(531)
70.95	0.5353	1.32715	(610)
74.28	0.102	1.27572	(620)
77.51	0.0816	1.23049	(533)

b. $ZnCo_2O_4$

Angle (2θ)	FWHM value	d-spacing (A^0)	hkl values
19.071	0.4014	4.65358	(111)
31.475	0.2676	2.84451	(220)
37.121	0.2676	2.42197	(311)
39.947	0.5353	2.2569	(222)
45.068	0.5353	2.01149	(400)
55.889	0.2676	1.64488	(422)
59.599	0.4015	1.55146	(511)
65.186	0.4015	1.43118	(440)
68.35	0.4014	1.37233	(531)
71.1385	0.4015	1.32537	(610)
74.242	0.5353	1.27743	(620)
77.549	0.66912	1.231	(533)

c. rGO

Angle (2θ)	FWMH value	d-spacing (A^0)	hkl values
25.65	0.401472	3.46557	(002)
43.3	0.802944	2.08848	(111)

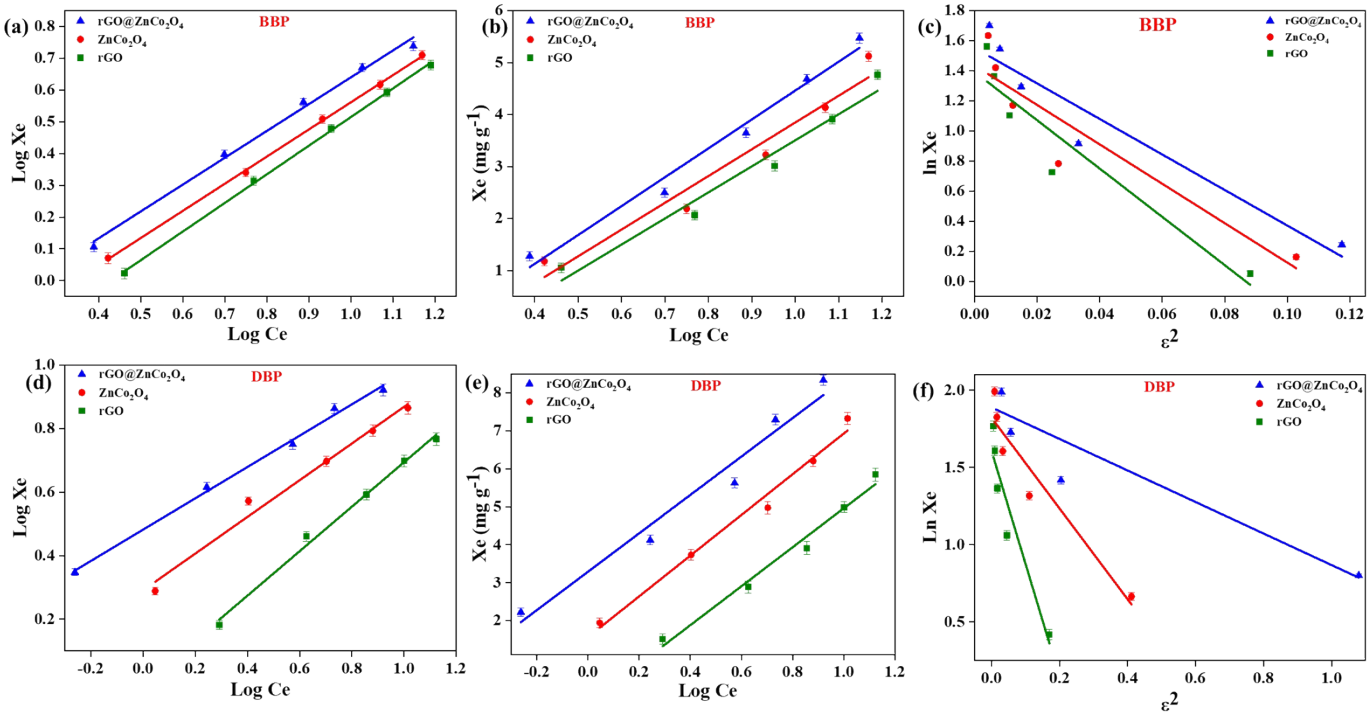

Figure 3S: (a, d) Freundlich (b, e) Temkin and (c, f) D-R isotherms for BBP and DBP PAEs adsorption. *Note: Triplicate experiments (n=3) were evaluated for estimation of error bar*

Table 2S. Comparison of different isotherms on the basis of R^2 and p values for BBP and DBP adsorption

	Langmuir				Temkin			
	BBP		DBP		BBP		DBP	
Catalyst	**R^2**	**p**	**R^2**	**p**	**R^2**	**p**	**R^2**	**p**
rGO@$ZnCo_2O_4$	0.9952	0.03	0.9943	0.03	0.99088	0.04	0.9852	0.04
$ZnCo_2O_4$	0.9928	0.03	0.99364	0.03	0.97524	0.04	0.9928	0.04
rGO	0.9856	0.03	0.99786	0.03	0.98235	0.04	0.99038	0.04

	DRK		Freundlich	
	BBP	DBP	BBP	DBP

Catalyst	R^2	p	R^2	p	R^2	p	R^2	p
rGO@$ZnCo_2O_4$	0.95031	0.03	0.96339	0.03	0.99677	0.03	0.99788	0.03
$ZnCo_2O_4$	0.93195	0.03	0.95789	0.03	0.99976	0.03	0.99184	0.03
rGO	0.9461	0.03	0.95119	0.03	0.99958	0.03	0.99706	0.03

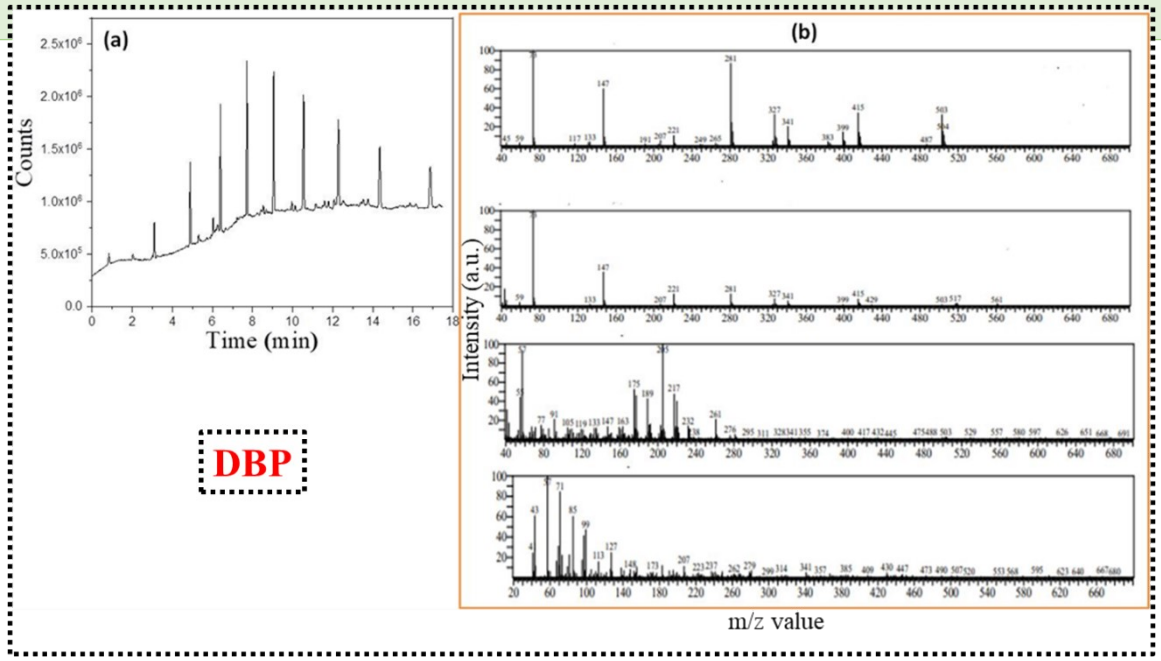

Figure 4S: GC-MS analysis with (a) TIC and (b, c, d) MS of some peaks of treated BBP sample

Figure 5S: LC-MS analysis with (a) TIC and (b) MS of some peaks of treated DBP sample

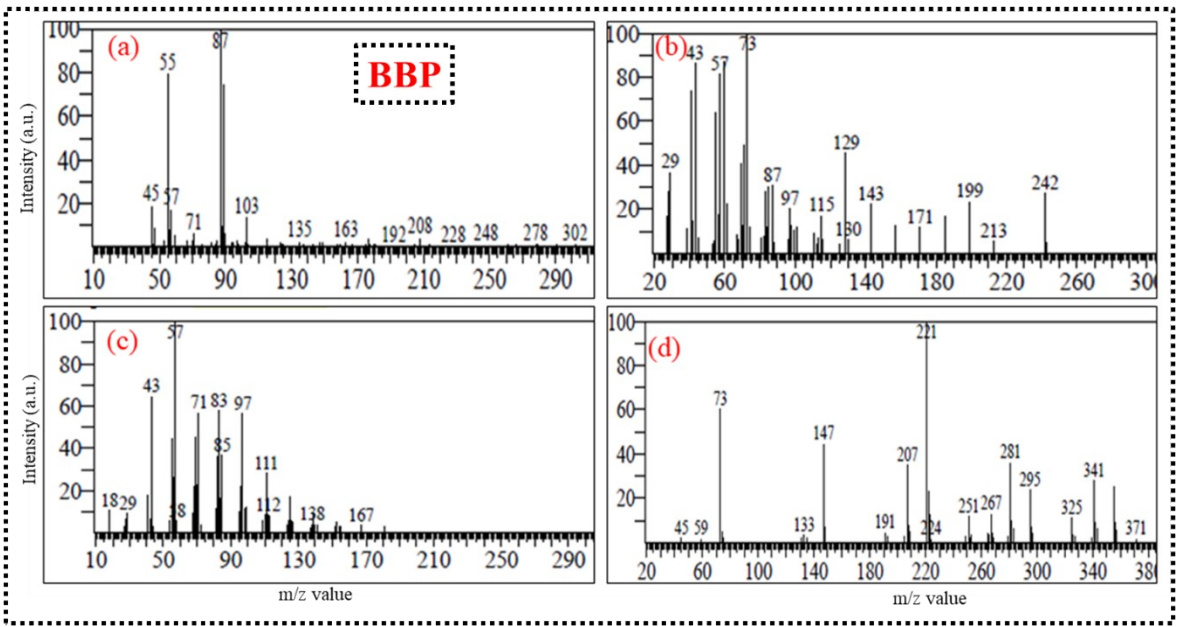

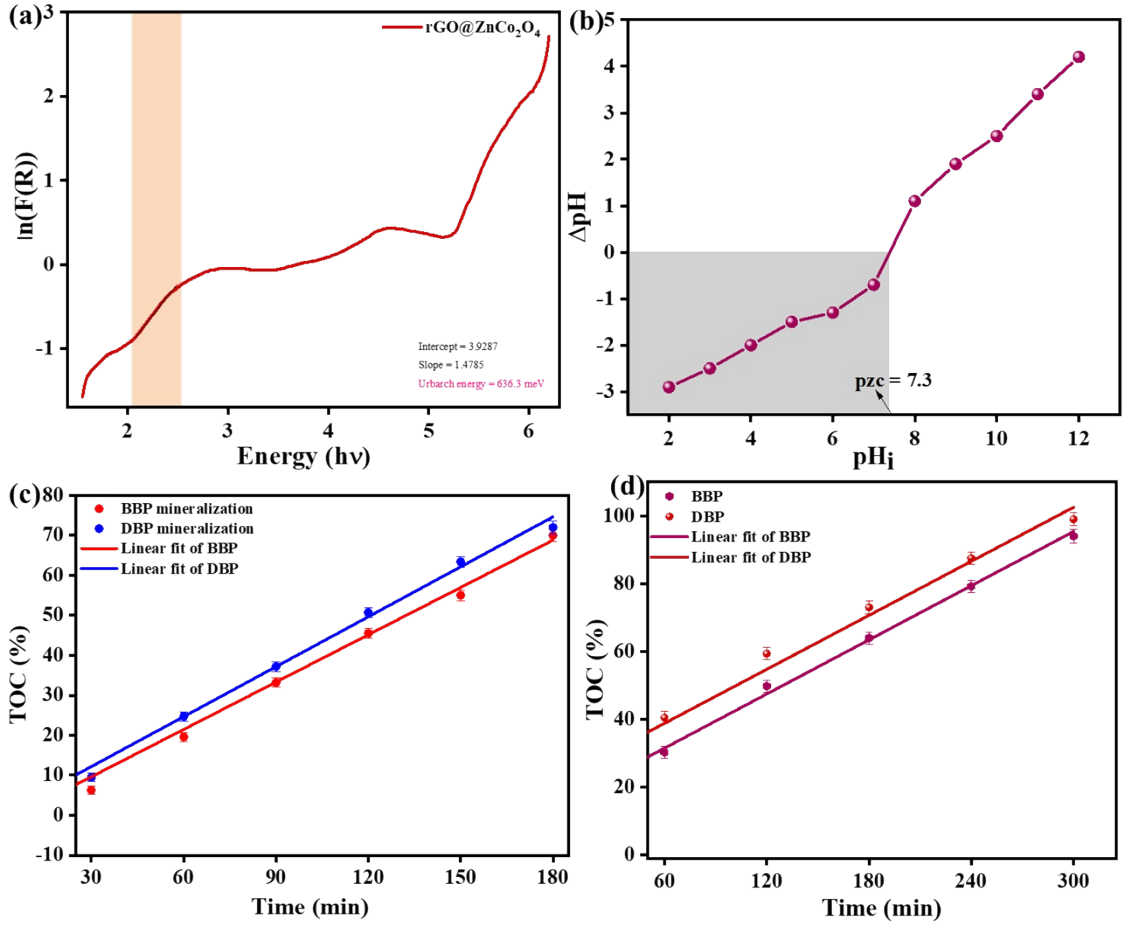

Figure 6S: (a) Urbach energy slope calculation, (b) PZC calculation of synthesized nanocomposite, (c,d) TOC analysis and mineralization efficiency of targeted PAEs (BBP and DBP) over the rGO@$ZnCo_2O_4$

Text S5: Turn over frequency (TOF)

As we know that TOF of catalysts determines their efficiency, i.e. higher the TOF more efficient is the catalyst. TOF value can be calculated with the help of following formula:

$$TOF = \frac{No\ of\ moles\ of\ reactant/No\ of\ grams\ of\ photocatalysts}{Time\ (min)} X\ yield$$

No. of gram of photocatalyst: 0.02 g. (5ppm)

Table 3S: TOF of rGO, $ZnCo_2O_4$ and rGO@$ZnCo_2O_4$ for BBP and DBP pollutants

S.No.	Photocatalyst	TOF (mol min^{-1} g^{-1})	
		BBP	DBP

1.	rGO@$ZnCo_2O_4$	4.27×10^{-6}	4.82×10^{-6}
2.	$ZnCo_2O_4$	3.6×10^{-6}	4.18×10^{-6}
3.	rGO	3.1×10^{-6}	3.58×10^{-6}

Table 4S: Reduced chi square and Adjusted R square values of kinetics model for BBP and DBP pollutant

	rGO@$ZnCo_2O_4$			**$ZnCo_2O_4$**			**rGO**			**Blank**		
Catalyst	**Adj. R^2**	**Red. Chi^2**	**DOF**	**Adj. R^2**	**Red. Chi^2**	**DOF**	**Adj. R^2**	**Red. Chi^2**	**DOF**	**Adj. R^2**	**Red. Chi^2**	**DOF**
BBP	0.99977	1.01339E-4	5	0.99684	3.43733E-4	5	0.99183	2.19033E-4	5	0.96832	1.36811E-4	5
DBP	0.99977	3.62289E-4	5	0.9996	2.55001E-4	5	0.99864	4.21659E-4	5	1	1.65978E-9	5

Table 5S: Reduced chi square and Adj. R square values of kinetics model for BBP and DBP pollutant

	Langmuir						**Temkin**					
	BBP			**DBP**			**BBP**			**DBP**		
Catalyst	**Adj. R^2**	**Red. Chi^2**	**DOF**	**Adj. R^2**	**Red. Chi^2**	**DOF**	**Adj. R^2**	**Red. Chi^2**	**DOF**	**Adj. R^2**	**Red. Chi^2**	**DOF**
rGO@$ZnCo_2O_4$	0.99804	0.66409	4	0.98579	0.60556	4	0.9758	7.94761	3	0.96083	15.00262	3
$ZnCo_2O_4$	0.98214	0.00178	4	0.98414	0.00265	4	0.93479	0.15789	3	0.98087	0.08456	3
rGO	0.96445	0.00327	4	0.99465	0.00121	4	0.95335	0.10029	3	0.97447	0.07443	3

	DRK	**Freundlich**

	BBP			DBP			BBP			DBP		
Catalyst	**Adj. R^2**	**Red. Chi^2**	**DOF**	**Adj. R^2**	**Red. Chi^2**	**DOF**	**Adj. R^2**	**Red. Chi^2**	**DOF**	**Adj. R^2**	**Red. Chi^2**	**DOF**
rGO@ZnCo$_2$O$_4$	0.87079	232.2761	3	0.90415	87.37674	3	0.99141	2.9116	3	0.99435	0.47979	3
ZnCo$_2$O$_4$	0.82 47	0.05908	3	0.89006	0.0299	3	0.99936	4.08285E-5	3	0.97832	0.00111	3
rGO	0.86013	0.04982	3	0.87301	0.036	3	0.99889	7.47148E-5	3	0.99216	4.19169E-4	3

Here DOF represents to degree of freedom.

Table 6S: The reaction rate constant values between reactive oxidative species and specific quenchers have been described below:

a) For BBP pollutant

Quenchers	Ct/Co	ln C_t/C_o	K (min^{-1})
Control	0.45	-0.7985077	0.00443615
t-BuOH	0.92	-0.08338161	0.00046323
p-BZQ	0.75	-0.28768207	0.00159823
Na_2EDTA	0.57	-0.56211892	0.00312288

b) For DBP pollutant

Quenchers	Ct/Co	ln C_t/C_o	K (min^{-1})
Control	0.26	-1.34707365	0.00748374
t-BuOH	0.89	-0.11653382	0.00064741
p-BZQ	0.65	-0.43078292	0.00239324
Na_2EDTA	0.53	-0.63487827	0.0035271

Table 7S: Composition of collected water samples

Parameters	Concentration
BOD_5 (mg/L)	10941.2
COD(mg/L)	1643.5

Total nitrate (mg/L)	149.1
Total Phosphate(mg/L)	527.6
pH	7.21
Chlorides (mg/L)	321.5
TDS (mg/L)	14823
Lead (mg/L)	0.9

Parameter	Untreated water	After DBP degradation	After BBP degradation	Tentatively identified byproducts (from literature)
Initial BBP concentration (mg L^{-1})	42.3	–	–	–
Initial DBP concentration (mg L^{-1})	51.2	–	–	–
Residual DBP (mg L^{-1})	–	13.36	–	Mono-butyl phthalate, phthalic acid, benzoic acid, formic acid, acetic acid
Residual BBP (mg L^{-1})	–	–	14.96	Benzyl phthalate, phthalic acid, benzoic acid, formic acid, acetic acid
COD (mg L^{-1})	95.2	27.5 (71% reduction)	30.1 (68% reduction)	–
TOC (mg L^{-1})	28.6	8.0 (72% reduction)	8.5 (70% reduction)	–
pH	7.4	7.1	7.2	–
Conductivity (µS cm^{-1})	320	305	308	–

Cadmium (mg/L)	1.3

Table 8S: Identified intermediates via LC-MS

Retention time (min)	Ionization mode	Observed m/z	Proposed formula	Assigned compound	Role in pathway

3.05	ESI^+	221.10	$C_{12}H_{14}O_4$	Monobutyl phthalate (MBP)	Primary hydrolysis of DBP
3.90	ESI^+	255.08	$C_{15}H_{14}O_4$	Monobenzyl phthalate (MBzP)	Primary hydrolysis of BBP
4.67	ESI^-	166.02	$C_8H_6O_4$	Phthalic acid	Ring oxidation intermediate
5.15	ESI^-	122.03	$C_7H_6O_2$	Benzoic acid	Aromatic ring oxidation
6.10	ESI^-	60.02	$C_2H_4O_2$	Acetic acid	Terminal degradation product
6.57	ESI^-	45.02	CH_2O_2	Formic acid	Final oxidative byproduct

References

[S1] Igara, C. E., D. A., Omoboyowa, A. A., Ahuchaogu, Orji, N.U., Ndukwe, M.K., 2016. Phytochemical and nutritional profile of Murraya koenigii (Linn) Spreng leaf. J. Pharmacognosy and Phytochemistry, 5

[S2] Ashtaputrey, S. D., Ashtaputrey, P. D., & Yelane, N. (2017). Green synthesis and characterization of copper nanoparticles derived from Murraya koenigii leaves extract. J. Chem. Pharm. Sci, 10(3), 1288-91.

[S3] Tudu, B., Nalajala, N., Reddy, K.P., Saikia, P., Gopinath, C.S. (2019). Electronic integration and thin film aspects of Au–Pd/rGO/TiO2 for improved solar hydrogen generation. ACS Appl. Mater. Interfaces, 11, 32869–32878.

[S4] Ceniceros-Reyes, M. A., Marín-Hernández, K. S., Sierra, U., Saucedo-Salazar, E. M., Mendoza-Resendez, R., Luna, C., ... & Barriga-Castro, E. D. (2022). Reduction of graphene oxide by in-situ heating experiments in the transmission electron microscope. *Surfaces and Interfaces*, *35*, 102448.

[S5] T. Chellapandi, N. Eswaramoorthy, N. Dineshbabu, S. Nallusamy, K. Pikon, and M. Ganesapillai, *Vacuum*, 2025, **239**, 114397.